INTERNATIONAL JOURNAL OF AUTOMOTIVE AND MECHANICAL ENGINEERING
ISSN: 2229-8649 e-ISSN: 2180-1606
VOL. 21, ISSUE 2, 2024, 11247 – 11262
DOI: https://doi.org/10.15282/ijame.21.2.2024.6.0869

RESEARCH ARTICLE

Computational Fluid Dynamics Evaluations on New Designs of the Delta-Shaped Blade Darrieus Hydrokinetic Turbine

K. Tantichukiad[1*], A. Yahya[1], A.M. Mustafah[1], A.S. Mohd Rafie[1], and A.S. Mat Su[2]

[1]Faculty of Engineering, Universiti Putra Malaysia, 43400 Selangor, Malaysia
[2]Faculty of Agriculture, Universiti Putra Malaysia, 43400 Selangor, Malaysia

ABSTRACT - In this research, the computational fluid dynamics (CFD) approaches using ANSYS Fluent solver was employed to evaluate new designs of the delta-shaped bladed Darrieus hydrokinetic turbines (DHKT) employing NACA0012 hydrofoils. The 2-bladed models with four different designs (*MD1-MD4*) of varying blade characteristics and cross-sectional areas were simulated. The models were positioned fully submerged inside a water flow domain and were forced to rotate with different rotational speeds by utilizing the sliding mesh technique under a constant upstream velocity of 1.5 m/s. The results using a Shear Stress Transport (SST) k-ω turbulence model were compared with previous studies. The optimum model designs were shown to be the models with twisted blades and reduced and constant cross-sectional areas (*MD3* and *MD4*). The 3-bladed models with similar blade characteristics (*MD7* and *MD8*) were continuously tested and compared with the 2-bladed models. The 2-bladed models performed better during the higher range of tip speed ratio (λ), whereas 3-bladed models were outstanding at the lower range. Based on the work using CFD approaches in this paper, the *MD4* model was shown to be the most appropriate design to operate under the specified conditions.

ARTICLE HISTORY
Received : 27th Apr. 2023
Revised : 17th Jan. 2024
Accepted : 08th Apr. 2024
Published : 20th June 2024

KEYWORDS
Turbine
Delta-shaped blade
In-plane blade
Twisted blade
CFD

1.0 INTRODUCTION

Currently, the emission of greenhouse gases has progressively increased due to the significant increase in electricity needs and energy consumption [1]. Renewable energy is a promising solution to solve global warming issues to help reduce dependency on fossil fuels. There are many kinds of renewable energy sources. Hydropower, however is more popular than others [2] thanks to its many advantages, especially in countries where there are ample irrigation networks. Hydropower generation is sustainable and reliable [3] because it has competitive costs, accepted efficiency [4] and minimal environmental impacts [5]. Besides, water levels and flow rate to use in hydropower generation systems are controllable [6], predictable, and measurable [7, 8]. The Darrieus hydrokinetic turbine (DHKT), categorized as a vertical axis turbine is a mechanical device used to generate electricity from running water in rivers flowing at between 0.5 and 2.5 m/s [9]. Initially, it was designed, developed, and proposed by a French engineer named Darrieus [10] and was used for almost a century. Darrieus turbine development started with simple designs, which included curved blades in 1968 and straight blades in the 1970s. It has the advantages of simple structure, low maintenance cost, energy capture independent of the direction of incoming flow, low noise, and environmental friendliness [11, 12].

Several experimental and computational studies on turbine geometric parameters for instance, rotor diameter [13], chord length [13, 14], blade thickness-to-chord [15], blade profiles [16 – 21], solidity [18, 21, 22], pitch angles [20, 21, 23, 24], aspect ratios [21, 25 – 27], number of blades [19, 21, 28], and blade shapes including the popular H-shape, helical-shape [29], egg-shape or ϕ-shape [30], J-shape turbines [31 – 33] were conducted. The studies showed that a general Darrieus turbine provides better efficiency at higher operational ranges (tip speed ratio) than other turbine types but suffers from the problems of self-starting [34 – 36] and also suffers from high cyclic fluctuation [37].

A lot of research activity was also conducted on the turbine blade modifications and passive flow control techniques, including the slotted airfoil [38, 39], a slotted deflective flap at the trailing edge [40, 41], the airfoil with different trapped vortex cavities layouts [42, 43], dimple designs and configurations [44, 45], leading-edge airfoil-slat [46], and the Gurney flaps [47, 48] in order to delay flow separation across the turbine blades and enhance their performance. The results showed that blade modifications could delay stall and enhance turbine power coefficient by around 18-28%.

Many series of blade profiles including NACA 00XX, NACA 63XXX, S-series, A-series, and FX-series with 20 different symmetrical and non-symmetrical airfoil shapes were investigated using two-dimensional computational fluid dynamics (CFD) approaches by Mohamed, 2012 [16]. The results found that the turbines with symmetric profiles provided a higher power coefficient (c_p) than the ones with non-symmetric profiles. Among those series, the S-1046 profile showed the highest maximum c_p.

Different aspect ratios of Darrieus turbines have also been investigated. It was found that an aspect ratio of 1.0 showed the highest c_p [26, 49]. Many researchers tested the number of blades. The results showed that the highest c_p was of a 2-

*CORRESPONDING AUTHOR | K. Tantichukiad | ✉ komsan.ta@udru.ac.th

bladed turbine [19, 50]. In addition, the c_p of the higher number of turbine blades was lower during a higher range of tip speed ratio [21]. Increasing turbine solidity by increasing the blade number lowers the power coefficient peak. At a high rotational speed, the lower number of turbine blades experienced less blade-to-blade interaction, which enhanced the turbine performance. However, the turbines with a higher number of blades had lower efficiency because each blade wake was not replaced with the clean stream rapidly; therefore, the subsequent blade had no efficient angle of attack to create a lift force [21].

The performance of Darrieus turbines with different blade shapes, including straight-blade, curved-blade, and helical-blade, was also determined by Scheurich and Brown, 2013 [51]. The study showed that the power loss experienced by the straight-bladed turbine was higher than the turbines with curved and helically twisted blades. Because the turbines with straight and curved blades have a variation of c_p with tip speed ratio that exhibits a steeper gradient in the mid-operating range than the one with helically twisted blades. Each blade section of the helically twisted blads achieves its highest individual aerodynamic performance [51]. Lee and Lim, 2015 [24] conducted numerical studies with four different values of helical angles, e.g., 0°(straight blade), 10°, 20°, and 30° by using 3-bladed NACA0018 Darrieus wind turbines. With small differences in the angle, the results showed that there was no significant influence on power performance [24].

The vorticity distribution, which was produced by straight-, curved-, and helical-bladed turbines, was also considered by Scheurich et al., 2010 [52]. It was found that the untwisted blades of the straight- and curved-bladed turbines caused a relatively symmetric distribution of vorticity in the wake downstream of the turbine. A strong asymmetry in the distribution between the upper and lower halves was observed in the turbine with helically twisted blades.

Aside from turbine geometric parameters, turbine arrangement and wake studies [53 – 55], installation of fixed guiding walls and upstream deflectors [56 – 58], or even the effect of an auxiliary or a double-bladed Darrieus turbine [21, 59 – 62] utilizing wind or hydro turbines have been investigated since then with the similar purpose of enhancing the turbine performance.

Most experimental and numerical research works on the performance of the Darrieus turbines have been carried out with straight-bladed, curved-balded, J-shape-bladed, and helical-bladed Darrieus turbines, as mentioned before. There was no information or study on the turbine with the delta-shaped blade. The current study thereby aims to evaluate the new delta-shaped blade DHKT designs through CFD analysis for geometric characteristics, including blade shapes (in-plane and twisted), blade cross-sectional areas (reduced and constant), and number of blades.

2.0 CONCEPTUAL MODEL DESIGNS

Several geometric parameters were determined based on previous studies to design the DHKT models. The blade designs were the main concern in this study. Firstly, blade profiles were considered from the literature for two reasons: either because they provided the most optimized performance or because they were found to be lacking. On consideration, a symmetrical NACA0012 profile, which had the pivot point located at a 0.2c unit from the frontal edge, as shown in Figure 1(a) was selected to utilize as a blade profile for all models due to the last reason. Additionally, blade shapes were also considered for a similar reason. Plenty of computational or experimental research works have been carried out using turbines with straight blades, also known as H-shaped blades [4, 16, 17]. However, studies on turbines with delta-shaped blades have been found lacking. The delta-shaped blade was accordingly selected.

Based on designs of blade shapes, there were two designs of the delta-shaped blade. The blade created from the normal NACA0012 profile illustrated in Figure 1(b) was called an in-plane delta-shaped blade. The blade created from the bent NACA0012 profile, as shown in Figure 1(b), was arranged along the circular line of the turbine system and was called a twisted delta-shaped blade. The blade designs of an in-plane and a twisted delta-shaped blade are illustrated in Figure 1(c) and (d), respectively.

The models consisted of three main parts: a central shaft, supporting arms, and delta-shaped blades. The blades were connected to a central shaft by supporting arms, as depicted in Figure 2. All supporting arms were also shaped as a NACA0012 profile. The shape and size of the supporting arm, as well as the shaft design, were kept constant to avoid any effect from those factors. The models' relative position was represented by azimuth angle (θ). Blade shapes were symmetrical along the x-z plane. The incline-blade angle (γ) of 60^o was fixed.

Turbine blades were also modified with two different designs corresponding to the turbine cross-sectional area. First, the blades were composed of two trapezoidal wings whose cross-sectional areas were reduced constantly by the factor of 0.5 from the x-z plane. This meant that the cross-sectional areas at both ends of the wings were half of the area in the x-z plane. Second, the blades were composed of two constant cross-sectional area wings. The combination of those two designed parameters, blade shapes and cross-sectional areas, for the 2-bladed DHKT models, ended with four iterations which were called *MD1-MD4*.

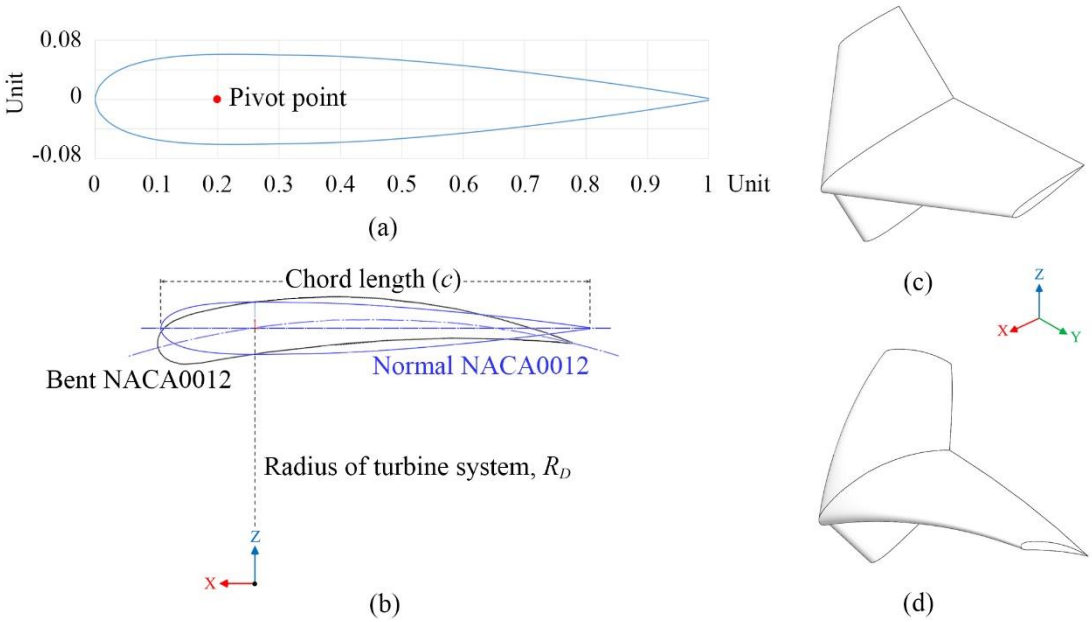

Figure 1. (a) NACA0012 profile, (b) Normal and bent NACA0012 profiles, (c) In-plane, and (d) Twisted delta-shaped bladed designs

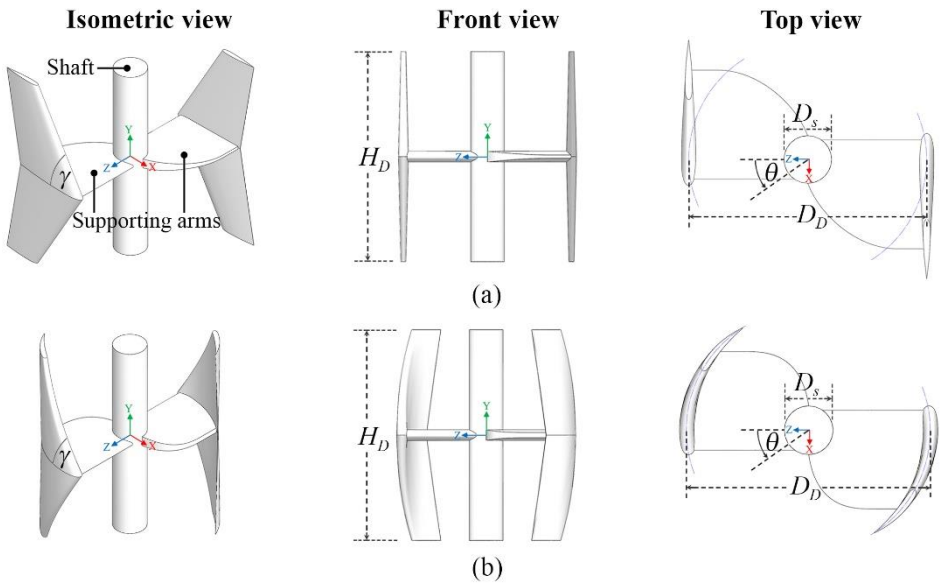

Figure 2. Schematic sketches of isometric, front, and top views of the 2-bladed (a) In-plane, and (b) Twisted delta-shaped blades with reduced cross-sectional area models

Design configurations of the *MD1-MD4* are presented in Figure 3, and the in-plane bladed models with reduced and constant cross-sectional areas are called *MD1* and *MD2*, respectively. Whereas *MD3* and *MD4* represented the twisted-bladed models with reduced and constant cross-sectional areas, respectively.

To investigate the effect of blade number, the DHKT models were also modified with four designs named *MD5-MD8*, as depicted in Figure 4. The model height (H_D) and diameter (D_D) were 0.15 m and 0.12 m, respectively, with the turbine aspect ratio of 1.25. As indicated from the literature, the Darrieus turbine performed better when an aspect ratio was greater than 1 [63]. The incline-blade angle (γ) was kept constant at 60°. The models were made from the Acylonitrile Butadiene Styrene (ABS) with a density of 1,020 kg/m^3. The general geometric parameters of a DHKT model are presented in Table 1.

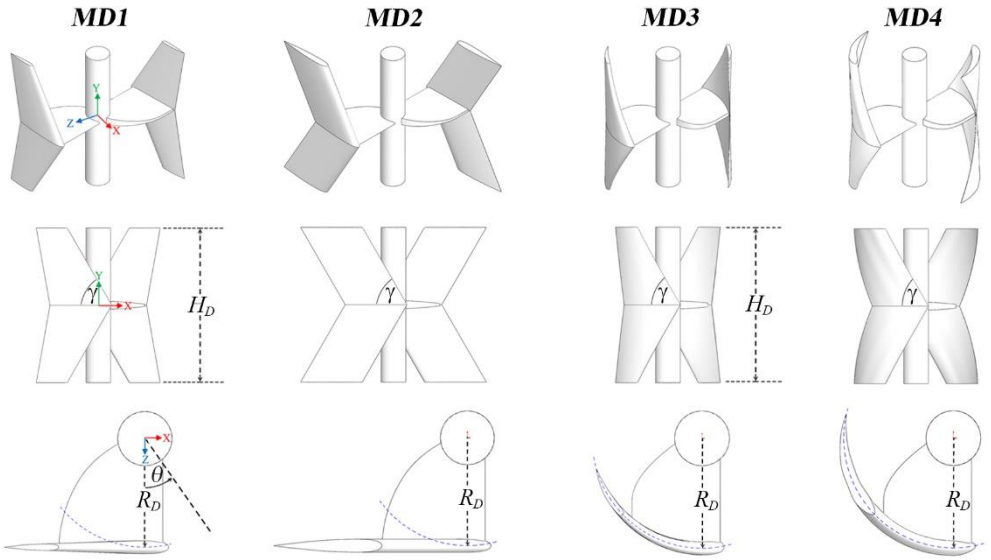

Figure 3. Design configurations of 2-bladed DHKT models (MD1-MD4)

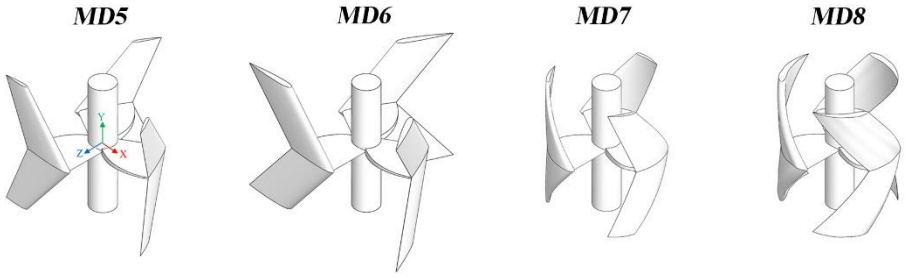

Figure 4. Designs of 3-bladed DHKT models

Table 1. Geometric features of DHKT models

Parameters	Values
Blade profile	NACA0012
Characteristic of blade	Delta-shaped blades
Number of blades, (n)	2, 3
Incline-blade angle (γ)	60^o
Chord length at Y = 0	0.10 m
Chord length at Y = 0.75 m.	0.05 m
Height (H_D)	0.15 m
Diameter (D_D)	0.12 m
Shaft diameter (D_s)	0.024 m
Turbine aspect ratio (H_D/D_D)	1.25
Material	ABS
Density of material	1,020 kg/m^3

3.0 OVERVIEW OF THE DHKT MODEL EVALUATION

CFD simulations were carried out using the ANSYS Fluent commercial software to evaluate the model designs and number of blades. There were two main parts of the evaluation as depicted in Figure 5. A general functional form as presented in Eq. (1) of each part followed and was introduced. The turbine performance, including coefficient of power (cp) and torque (ct), was the dependent variable (*DV*), while the tip speed ratio (λ) was an independent variable (*IV*). For the first part, four different designs of 2-bladed models (*MD1 – MD4*) were studied. Thus, the model designs had variable parameters (*VP*) and other parameters such as number of blades (n), incline-blade angle (γ), and upstream water velocity (U_∞) were kept as constant parameters (*CP*). A functional form of this part was in Eq. (2). After getting the results from the first part, the simulations were conducted continuously to evaluate the effect of the number of blades (n). The results of the model design evaluation from the previous part were compared with those of 3-bladed designs (n = 3), while the

rest of the parameters were fixed. A functional form of the second part was in Eq. (3). In order to make a fair comparison, the general specifications of the models were kept constant.

$$DV = f(IV\ ;\ VP\ ;\ CP) \tag{1}$$

$$c_p, c_t = f(\lambda\ ;\ MD1, MD2, MD3, MD4\ ;\ n = 2, \gamma = 60^o, U_\infty) \tag{2}$$

$$c_p, c_t = f(\lambda\ ;\ n = 2, n = 3\ ;\ MD, \gamma = 60^o, U_\infty) \tag{3}$$

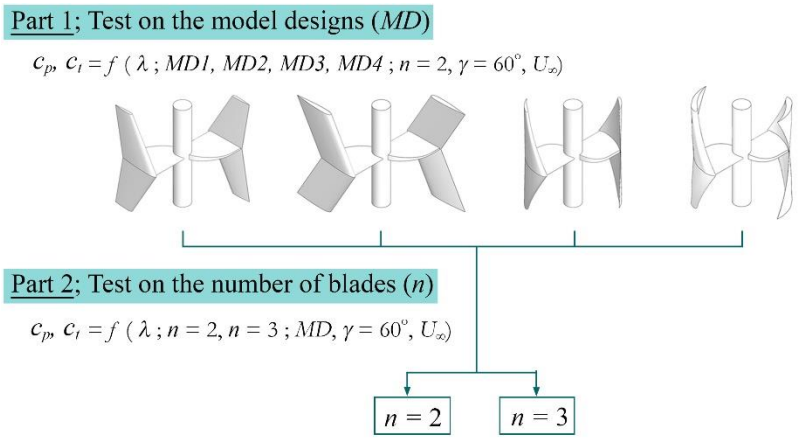

Figure 5. Evaluation procedures

4.0 COEFFICIENT OF PERFORMANCES

Turbine performances can be identified by two dimensionless parameters. The first one is the power coefficient (c_p), defined as a ratio of the actual mechanical power (P_m) generated by a DHKT rotor to the available hydropower (P_{Hydro}) as expressed in Eq. (4) and the second one is torque coefficient (c_t) expressed as Eq. (5) which represented the net dynamic torque produced from all blades of the rotor at a particular rotor angle. Besides, the relationship between c_p and c_t is derived in Eq. (6), where λ is called a tip speed ratio (TSR). λ defined as a ratio of tip speed, or tangential velocity (v) of a turbine blade to the speed of the upcoming water (U_∞) is a dimensionless parameter used to distinguish turbine performances. Mainly, the c_p and c_t of general hydrokinetic turbines rely on TSR. In fact, for constant upstream flow, lower TSR means that a turbine rotor rotates considerably more slowly and allows medium fluids to flow through the open spaces between turbine blades with little extracted power. On the other hand, when a turbine rotor rotates too fast, the rotating blades behave as a solid obstruction blocking the flow and accordingly decreasing the extracted power.

$$c_p = \frac{P_m}{P_{Hydro}} = \frac{\tau\omega}{0.5\rho U_\infty^3 H_D D_D} \tag{4}$$

$$c_t = \frac{4\tau}{\rho H_D D_D^2 U_\infty^2} \tag{5}$$

$$\lambda = \frac{c_p}{c_t} = \frac{v}{U_\infty} = \frac{\omega D_D}{2U_\infty} \tag{6}$$

5.0 COMPUTATIONAL APPROACH

The ANSYS Fluent commercial software based on the finite volume method was utilized to carry out all 3D simulations in this study. The water flow around the DHKT models was assumed to be three-dimensional, turbulent, and transient incompressible fluid flow. The time-dependent Unsteady Reynolds-Averaged Navier Stokes (URANS) equations with the pressure-based formulation were solved with the pressure-velocity coupling solution scheme using the Semi-Implicit Method for Pressure Linked Equation (SIMPLE) algorithm. Besides, the spatial discretization of the pressure, momentum, and turbulence equations was employed with the second-order upwind scheme. The governing equations including the continuity and momentum equations of the flow for unsteady Newtonian incompressible turbulent flow were given in Eq. (7) and (8) by index notation.

$$\frac{\partial \overline{u}_i}{\partial x_i} = 0 \tag{7}$$

$$\frac{\partial \overline{u}_i}{\partial t} + \overline{u}_j \frac{\partial \overline{u}_j}{\partial x_j} = -\frac{1}{\rho}\frac{\partial \overline{P}}{\partial x_i} + \frac{\mu}{\rho}\frac{\partial^2 \overline{u}_i}{\partial x_j^2} - \frac{\partial}{\partial x_j}(\overline{u'}_i \overline{u'}_j) \tag{8}$$

There was no agreement on the most appropriate turbulence model adopted in CFD simulations. However, according to previous studies, the Shear Stress Transport (SST) *k-ω* turbulence model, which was a hybrid model consisting of the *k-ε* and *k-ω* combination has abilities to capture flow structures in the boundary layer as well as the free stream regions [17]. It has been widely used in the simulations of vertical axis turbines and showed good agreement with experimental measurements [16, 50]. Hence, the SST *k-ω* turbulence model was utilized for all simulations as an acceptable model to consider the performances and flow characteristics of the DHKT models. The transport equation for the SST *k-ω* can be written as Eq. (9) and (10).

$$\frac{\partial}{\partial t}(\rho k) + \frac{\partial}{\partial x_j}(\rho k u_j) = \frac{\partial}{\partial x_j}\left[\left(\mu + \frac{\mu_t}{\sigma_k}\right)\frac{\partial k}{\partial x_j}\right] + G_k - Y_k \tag{9}$$

$$\frac{\partial}{\partial t}(\rho \omega) + \frac{\partial}{\partial x_j}(\rho \omega u_j) = \frac{\partial}{\partial x_j}\left[\left(\mu + \frac{\mu_t}{\sigma_\omega}\right)\frac{\partial \omega}{\partial x_j}\right] + G_\omega - Y_\omega \tag{10}$$

where k, ω, μ, μ_t were turbulent kinetic energy, specific dissipation rate, molecular viscosity of a fluid, and turbulent viscosity. Besides, G_ω and Y_ω represent generation of ω and dissipation of turbulence kinetic energy, respectively.

In order to obtain an accurate result, a time step size (Δt) was determined by the azimuthal increment. For the sliding mesh technique, Δt was calculated based on the degree of revolutions. This meant that the unit time step was equal to the time that a turbine rotated at one degree. Hence, the time step size was varied depending on the desired rotational speed (ω_o) of the models or λ. The appropriate Δt was considered by using the time step independence study. Based on the previous study, the Δt 0.5° rotation was precise enough [16, 19] and acceptable to use as a time step size for all simulations. The Δt of 0.5° increment can be calculated by Eq. (11).

$$\Delta t\ (0.5^\circ) = \frac{\pi}{360\omega_o} \tag{11}$$

The convergence criteria were imposed to be 10^{-5} for the residual of all equations including continuity and momentum equations. The maximum iterations were set as 100 per Δt. The simulations were run until the results were converged. In order to consider the convergence, the repeated average power coefficient ($c_{p,avg}$) of each revolution was calculated and determined. In fact, when the convergent criterion (ε) expressed in Eq. (12) was less than 1% [64] in at least two consecutive revolutions, it meant that the simulation results had already reached the convergence criterion. The solver setting for all simulations is presented in Table 2.

$$\varepsilon = \frac{c_{p,avg(n+1)}(\theta) - c_{p,avg(n)}(\theta)}{c_{p,avg(n)}(\theta)} < 1\% \tag{12}$$

Table 2. The solver setting for simulations of DHKT models

Parameters	Values
Turbulence model	SST *k-ω*
Pressure–velocity coupling Scheme	SIMPLE
Spatial Discretized	
-Pressure equation	Second order upwind
-Momentum equation	
-Turbulent kinetic energy k equation	
-Specific dissipation rate ω equation	
-Transient formulation	
Maximum iterations per time step	100
Convergence criterion	$\varepsilon < 1\%$
Residual	10^{-5}

5.1 Computational Domain

A computational domain depicted in Figure 6(a) was used for all simulation cases. It was created as a rectangular cube. Its dimensions were represented in the form of multiples of a model diameter (D_D) which were $10D_D$, $10D_D$ and

$23D_D$ in x-, y-, and z- directions, respectively. The DHKT model was positioned at the origin of a Cartesian coordinate system (0, 0, 0). It was $5D_D$ downward from the inlet boundary.

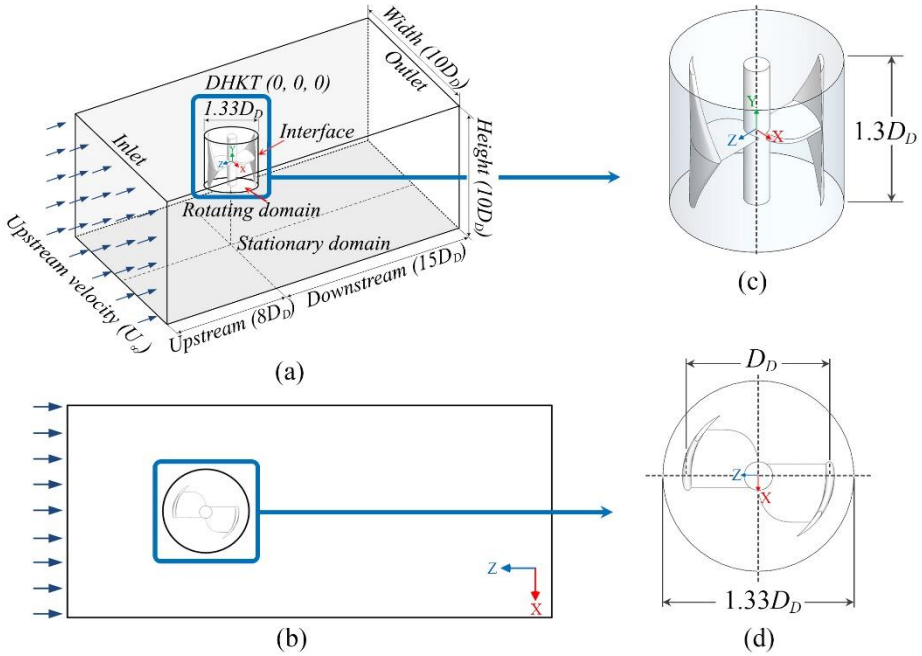

Figure 6. (a) Isometric view and geometric parameters of a rectangular computational domain, (b) top view, (c) isometric view of the rotating zone, and (d) top view of the rotating zone

The model initial position where $\theta = 0^{o}$ was illustrated in Figure 6(b). The domain comprised two main regions which were a stationary domain and a rotating domain surrounding the model. Both regions were separated by a rotating cylindrical surface, called an interface boundary, where the continuity of absolute velocity was set to ensure the continuity of the flow field and the rotating region was allowed to rotate freely with different rotational speeds whereas the rest was kept as fixed [23, 51]. The model was located inside and at the center of a rotating cylinder which has the diameter and height of $1.33D_D$ and $1.3D_D$, respectively as seen in Figure 6(c) and (d).

5.2 Boundary Conditions

The sliding mesh technique was employed for all simulations. For this technique, a model was forced to rotate constantly in the positive direction with different rotational speeds (ω_b) from 10 to 37.5 rad/s, under a constant upstream velocity (U_∞) of 1.5 m/s. In general, water flow characteristics in an irrigation canal were varied depending on canal geometries, hydraulic head, quantities of seasonal rainfall, etc. U_∞ of 1.5 m/s was selected in this study to consider the turbine performances in a high flow condition. The outlet total pressure was set as zero. The turbulence intensity (I) of 5% and turbulent viscosity ratio of 10 were imposed. For all surfaces of a model and flow channel, the standard wall roughness and non-slip condition were assumed. The boundary and initial conditions used for simulations of the DHKT models are represented in Table 3.

Table 3. Boundary and initial conditions of the 3D DHKT model simulations

Location	Boundary and initial	Condition	Value
Inlet	Velocity inlet	Uniform water flow, Normal to the boundary	1.5 m/s
Outlet	Pressure outlet	Total pressure	0 (gauge pressure)
Domain channel	No slip walls Stationary wall	Standard wall roughness	0.5
DHKT surfaces	No slip walls Stationary wall	Standard wall roughness Rotate at the setting	0.5
Flow condition	Turbulent intensity (I) Turbulent viscosity ratio		5% 10
Interface	The link of the rotating and stationary region		Coupled surface

5.3 Mesh Configuration and Independency Study

Mesh was generated by using the ANSYS-Mesh module. As mentioned, there were two different regions of a flow domain. In practice, mesh generation with the unstructured tetrahedral elements was set with different mesh densities in each region. In the rotating region, finer meshes were created than in the stationary region. To capture velocity and pressure gradients, inflation layers were applied to model surfaces. To achieve a maximum y^+ value of less than five over the near walls of the model, the first layer cell thickness of 0.5 mm was applied using a growth rate of 1.1 and total layers of 7.

The quality of the mesh significantly influenced the efficiency, accuracy and precision of CFD simulation [17]. To optimize mesh size or mesh resolution, an independent study was conducted with seven different mesh sizes, which varied from both regions. The mesh configuration details are presented in Table 4. The simulations were carried out until the results represented by the average c_p had already reached the convergence criterion, as mentioned in Eq. (9)

Table 4. Mesh independency study

Mesh	Element size (mm.)		Number of Nods		Number of Elements	
	Inner (MI)	Outer (MO)	Inner	Total	Inner	Total
M1	50	60	185,549	225,522	678,570	899,295
M2	50	50	185,481	253,094	677,767	1,056,926
M3	30	50	185,721	253,334	678,803	1,057,962
M4	30	40	185,548	316,075	678,103	1,418,068
M5	30	30	185,191	489,978	677,311	2,427,216
M6	20	30	185,492	490,279	677,333	2,427,238
M7	15	30	185,524	490,311	678,414	2,428,319

The simulations of the mesh independency study were conducted by using the *MD3* model together with the sliding mesh method. The model was forced to rotate with ω_o = 37.5 rad/s under constant U_∞ of 1.5 m/s (λ = 1.5). Variation of instantaneous c_p with flow time as illustrated in Figure 7(a) from all configurations was dramatically close. However, there were some differences, especially at the peaks. The peaks of M1 were a little bit higher than the rest. Besides, the results of M1-M7 showed that the average c_p of the 8th revolution already reached the convergence criterion. As seen in Figure 7(b), it was also found that the decreasing mesh size in the rotating region (MI) between M2 and M3, or M5 to M7 showed a smaller effect, while a change of size in the stationary region (MO) from M3 to M5 showed a huge effect on the predicted results. In addition, the average c_p of M1 to M6 was compared with M7 (finest mesh resolution) as a reference value. It was found that, the percentage differences (δ) of M4 - M6 were still close (δ < 1%) to M7. However, the average c_p of M3 was over the criterion value of 1%. Therefore, the M4 configuration was selected to be employed for all simulations. The mesh topology of the M4 configuration at different views using a 2-bladed DHKT model (*MD3*) is presented in Figure 8.

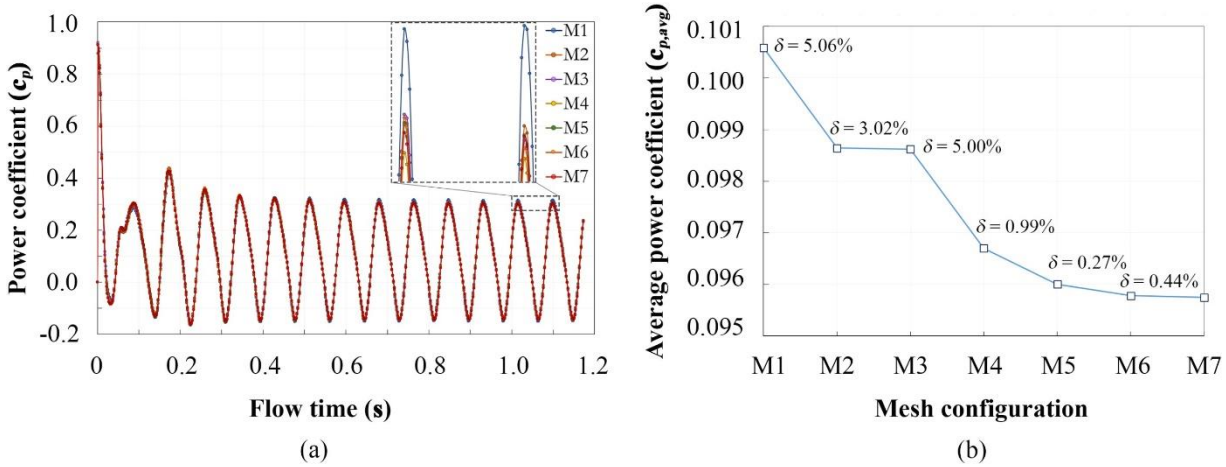

(a) (b)

Figure 7. (a) Variation of instantaneous c_p with flow time of several mesh configurations (M1-M7), and (b) The average c_p of 8th revolution of each mesh configuration and its percentage differences (δ)

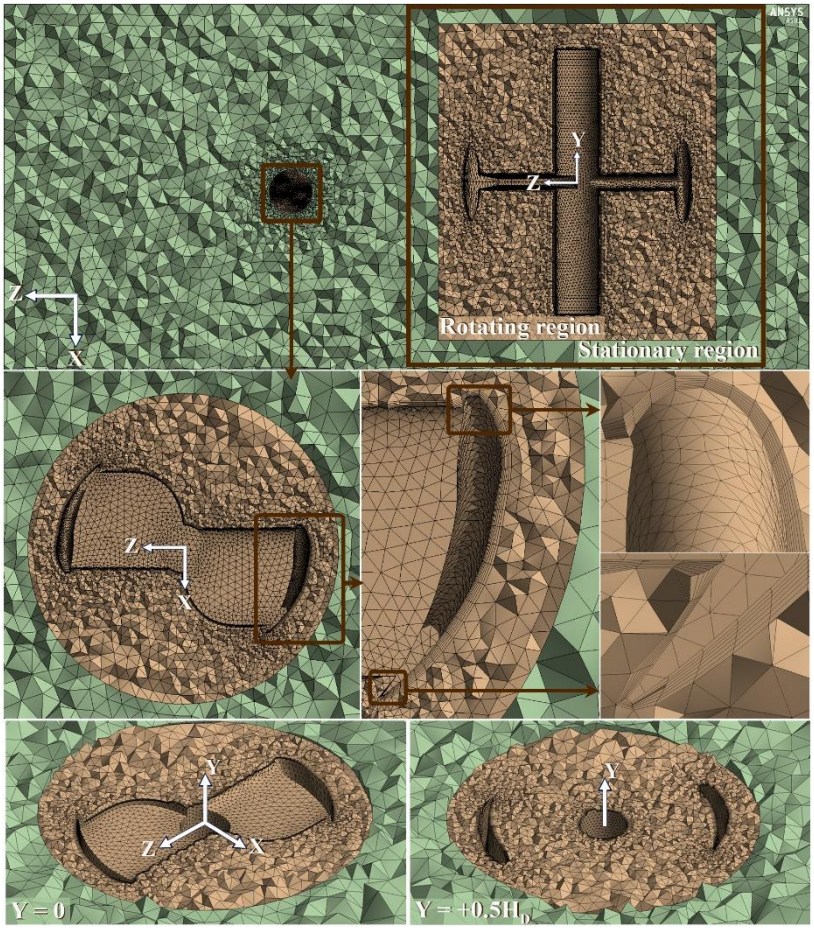

Figure 8. Mesh configuration of M4 (MI = 30 mm, MO = 40 mm)

6.0 SIMULATION RESULTS

6.1 Comparison of Simulation Results

The calculated c_p as a function of λ, *MD3* and *MD8* were compared with the previous numerical [13, 17] and experimental results [55], as shown in Figure 9. The previous results were investigated by utilizing the Darrieus hydro turbines and NACA0012 hydrofoils. The detailed specifications of those models are listed in Table 5. The numerical and experimental results from previous and present studies showed similar downward parabolic shapes. Each curve had a maximum c_p point that varied from approximately 0.05 to 0.20. However, there were some differences in the curves as well due to different test model designs, materials, sizes, test approaches, and flow conditions.

The simulation result of Yagmur et al., 2021 [17] was slightly higher than others because of using 2D simulation. In fact, 2D simulation did not consider the effects of the flow phenomenon at the end of turbine blades as well as the effects of shear flow at the top and bottom walls. Therefore, the c_p of a 2D simulation was overpredicted in contrast with the 3D simulation and experimental results [17]. Moreover, the operational ranges of λ from Tian et al., 2013 [13] were wider due to the longer diameter of the tested turbine.

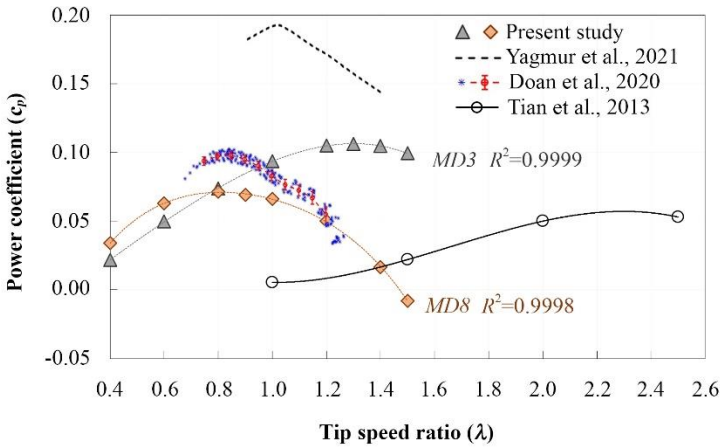

Figure 9. Comparison of simulation results

Table 5. Detailed specifications of the verification DHKT models using NACA0012 profile

Parameters	Tian et al., 2013 [13]	Yagmur et al., 2021 [17]	Doan et al., 2020 [55]	Present study
Method	2D Simulation	2D Simulation	Experiment	3D Simulation
Turbine Characteristics	Straight blade 3 blades	H-type blade 3 blades	Straight blade 3 blades	Delta-shaped blade 2, and 3 blades
Turbine size (H_D, D_D, c) (mm.)	(-, 2000, 150)	(-, 250, 100)	(100, 62.8, 25.4)	(150, 120, 100 at Y=0), (150, 120, 50 at Y=75)
Upstream velocity	0.5 m/s	0.46 m/s	0.316 m/s	1.5 m/s
Range of TSR	[1.0,2.5]	[0.9,1.4]	(0.6,1.3)	[0.4,1.5]
Maximum c_p	Not mentioned	0.182 (λ=1.0)	0.108 (λ=0.9)	0.106 (λ=1.3)

6.2 Effect of the Model Designs

Under the convergence criterion, variations of average c_p and c_t with λ for four different designs, *MD1* - *MD4* at a constant U_∞ of 1.5 m/s were depicted in Figure 10. As illustrated in Figure 10(a), c_p and c_t of *MD1* and *MD2* decreased as λ increased. Both designs always generated the negative torque direction over a complete cycle in every rotational position of the turbine. Hence c_p and c_t were also negative for all ranges of λ. On the other hand, c_p and c_t of *MD3* and *MD4* shown in Figure 10(b) increased with an increase of λ up to the maximum value of each and then c_p and c_t of both were down. The maximum c_p for *MD3* and *MD4* were about 0.1064 at λ = 1.3, and 0.1012 at λ = 1.2, respectively. Besides, the c_p and c_t of *MD4* were slightly higher than *MD3* when λ was lower than 1.0. Beyond λ = 1.0, c_p and c_t of *MD3* were clearly higher.

Figure 11 illustrates isometric views of velocity streamlines inside the inner domain of *MD1* - *MD4* designs when θ = 360º, ω_0 = 10 rad/s, and U_∞ = 1.5 m/s. The sections a-a and b-b illustrated in Figure 11 at Y = 0, and Y = +0.0375 m respectively, were used to present flow characteristics on the sections.

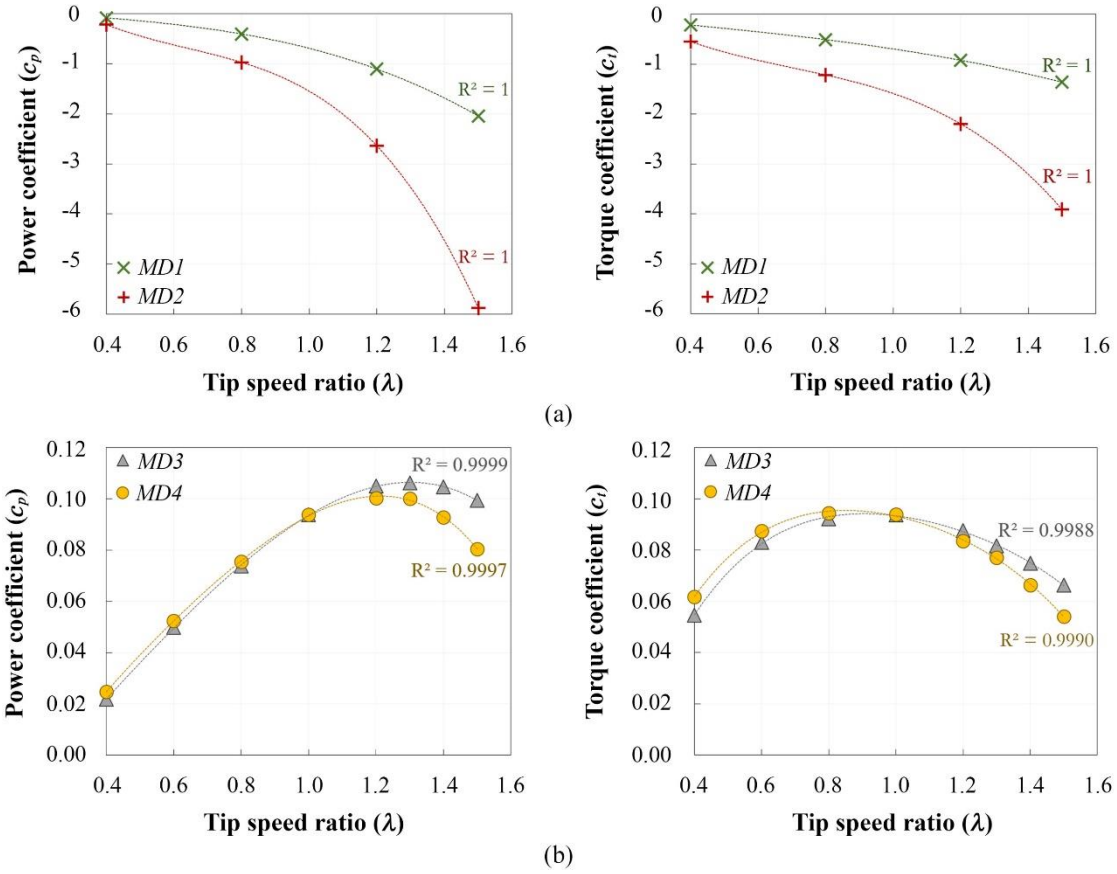

Figure 10. Variation of the average c_p and c_t versus λ of (a) *MD1* and *MD2*, and (b) *MD3* and *MD4*

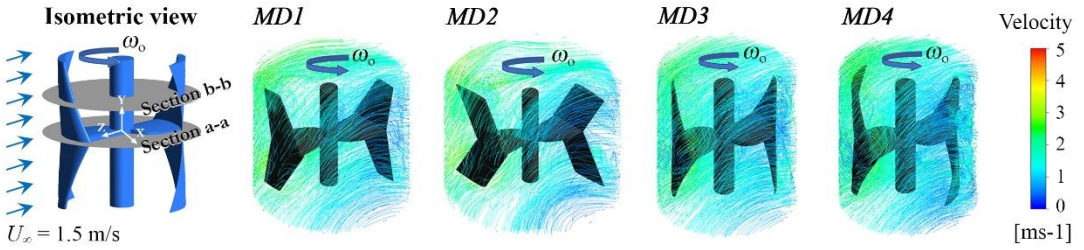

Figure 11. Isometric views of velocity streamlines inside the inner domain of the model designs, *MD1* - *MD4* when $\theta = 360^o$, $\omega_o = 10$ rad/s, and $U_\infty = 1.5$ m/s

Figure 12 shows the sectional total pressure contours along with velocity vectors of flow fields inside the inner domain at two different sections (section a-a, and section b-b) when $\theta = 0^o$ and 120^o, $\omega_o = 10$ rad/s, and $U_\infty = 1.5$ m/s. As seen in the figure, the higher-pressure regions could be observed at the leading edge and pressure side surface, where positive pressure was generated from an advancing blade for all designs and the pressure decreased after becoming a returning blade. At $\theta = 0^o$, an advancing blade of *MD1* and *MD2* was hit directly on the pressure side surface by upcoming water flow, while water flow could travel along the blade surface of *MD3* and *MD4*. It caused more adverse pressure gradients, and hence, dynamic stalls were generated at the trailing edges of *MD1* and *MD2*. Vortices detached from the leading and trailing edge could be observed clearly in section b-b, and they were bigger and wider for *MD1* and *MD2*.

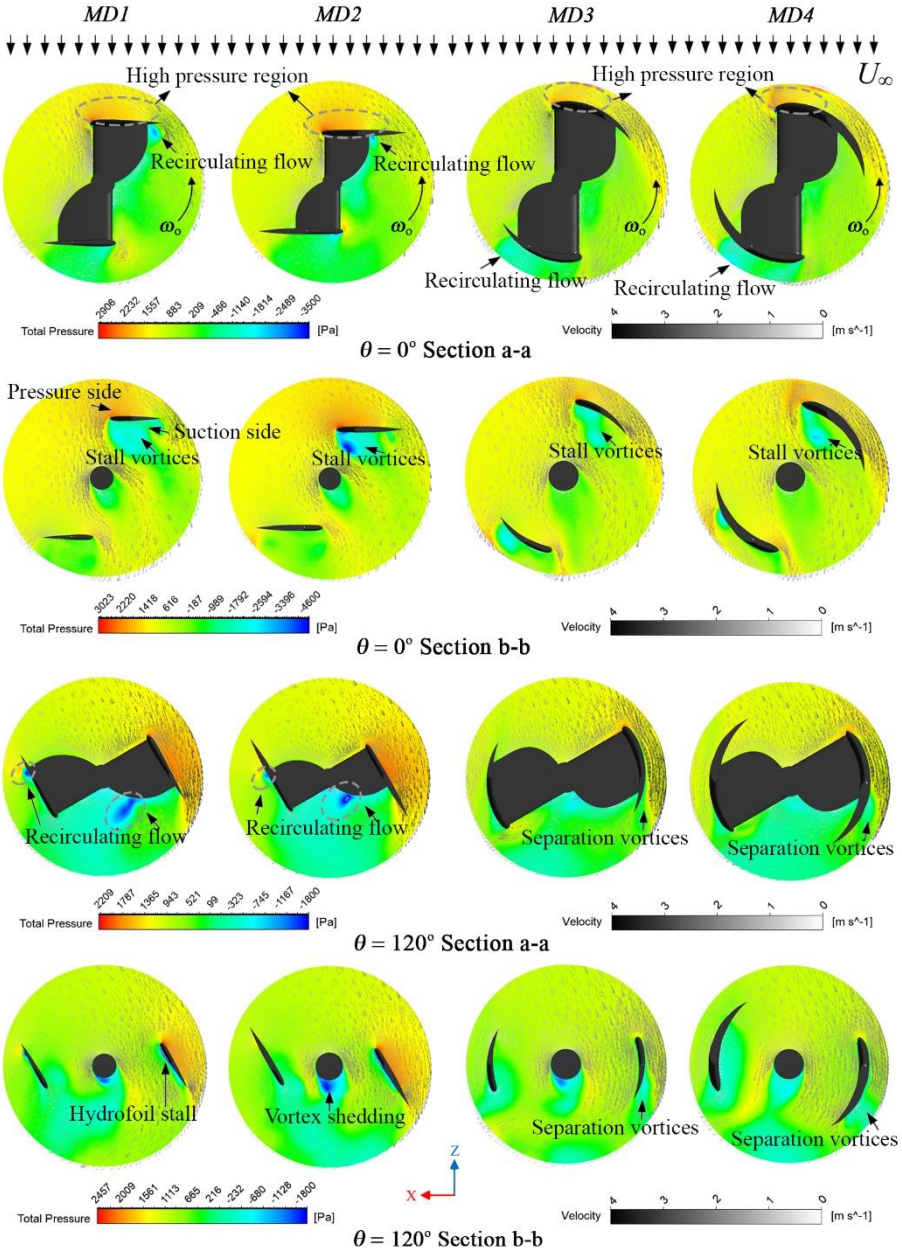

Figure 12. Sectional total pressure contours and velocity vectors inside the inner domain of the *MD1* – *MD4* designs when $\theta = 0^o$, and 120^o, $\omega_o = 10$ rad/s, and $U_\infty = 1.5$ m/s

When θ = 120º, the higher-pressure zone was seen for *MD1* and MD2 in both sections. Thin hydrofoil stalls and recirculating flow could also be observed for *MD1* and *MD2* due to the angle of attack of the blades. An advancing blade of *MD1* and *MD2* was acted on by water pressure and shear stress on its surface at the pressure side surface. Therefore, the negative torque value was generated and then negative c_p and c_t curves as shown in Figure 10(a) were produced for all rotational speeds. For the twisted blade designs (*MD3* and *MD4*), pressure distribution and flow behavior on both sections when θ = 0º, and 120º were almost similar. Flow separations at the trailing edge on the pressure side surface could be observed when θ = 120º on both sections. Vortices detached from the leading and trailing were observed on section b-b when θ = 0º, however, it was considerably smaller compared to the in-plane blade designs. Vortex shedding was also noticed behind the cylinder shaft in all models. Based on c_p and c_t curves and flow characteristics, *MD3* and *MD4* were selected for ongoing consideration of the effect of the number of blades.

6.3 Effect of the Number of Blades

By using similar bladed characteristics and model configurations, 3-bladed models, *MD7* and *MD8*, were selected. The *MD5* and *MD6* designs which used in-plane blades were eliminated because of negative torque generation. Under similar simulation approaches, and constant U_∞ of 1.5 m/s, the converged average c_p and c_t with respect to λ of 3-bladed models for each simulation were calculated and plotted together with the 2-bladed models as illustrated in Figure 13(a) and (b).

The converged average c_p and c_t curves for the 2-bladed models (*MD3* and *MD4*) and the 3-bladed models (*MD7* and *MD8*) were slightly different. As depicted in Figure 13, the c_p and c_t of *MD7* and *MD8* were higher than the ones of *MD3* and *MD4* when λ was lower than 0.8 approximately. Further increasing of λ beyond 0.8, *MD3*, and *MD4* provided higher c_p and c_t. Besides the number of blades, the cross-sectional areas of blades also affected turbine performance. During a low range of λ, the models with constant cross-sectional area blades, *MD4* and *MD8* showed higher c_p and c_t while the reduced cross-sectional area bladed models, *MD3* and *MD7* provided higher c_p and c_t during a high range of λ.

For 2-bladed models, the maximum c_p was 0.10623 at λ = 1.3 for *MD3*, and 0.10027 at λ = 1.2 for *MD4*. At the same time, the maximum c_p of 3-bladed models was found to be 0.07594 at λ = 0.9 for the *MD7*, and 0.07138 at λ = 0.8 for the *MD8*. Furthermore, the maximum c_t of *MD7* and *MD8* occurred at λ = 0.6 were around 0.10241, and 0.10519, respectively, while maximum c_t points of *MD3*, and *MD4* were 0.09380, and 0.09448 at λ = 1, and 0.8, respectively.

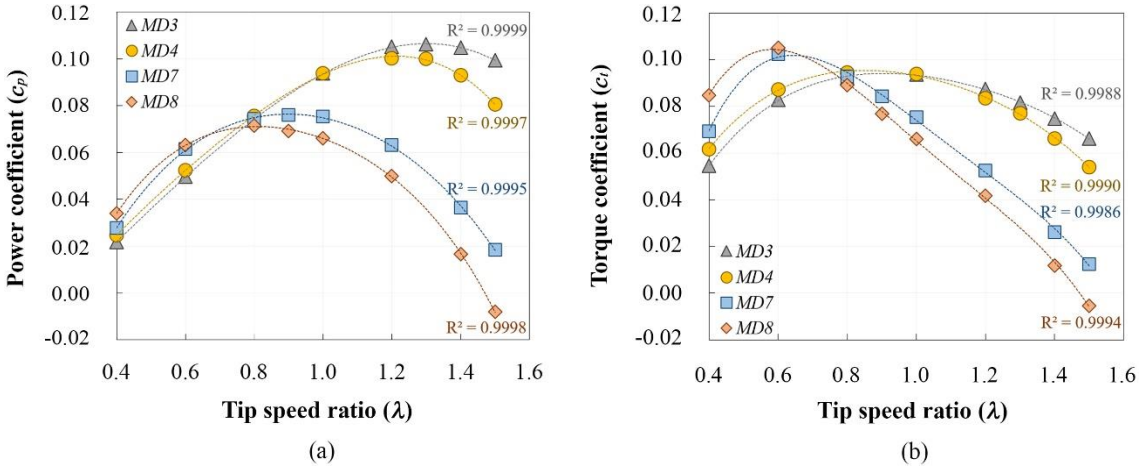

Figure 13. Variation of the converged average (a) c_p and (b) c_t with λ of 2-bladed (*MD3*, *MD4*), and 3-bladed (*MD7*, *MD8*) models

It could be observed that the 3-bladed models and models with constant cross-sectional area blades performed better during a low range of λ whereas the 2-bladed models and models with reduced cross-sectional area blades showed higher c_p, and c_t when λ was higher. The maximum c_p occurred when ω_o = 32.5, 30, 22.5, and 20 rad/s for *MD3*, *MD4*, *MD7*, and *MD8* respectively. It was the maximum operational condition for those models. Flow visualization represented by isometric views of velocity streamlines, velocity and pressure contours inside the inner domain of the models at the maximum operational condition when θ = 360º, and U_∞ = 1.5 m/s were presented in Figure 14, and Figure 15, respectively.

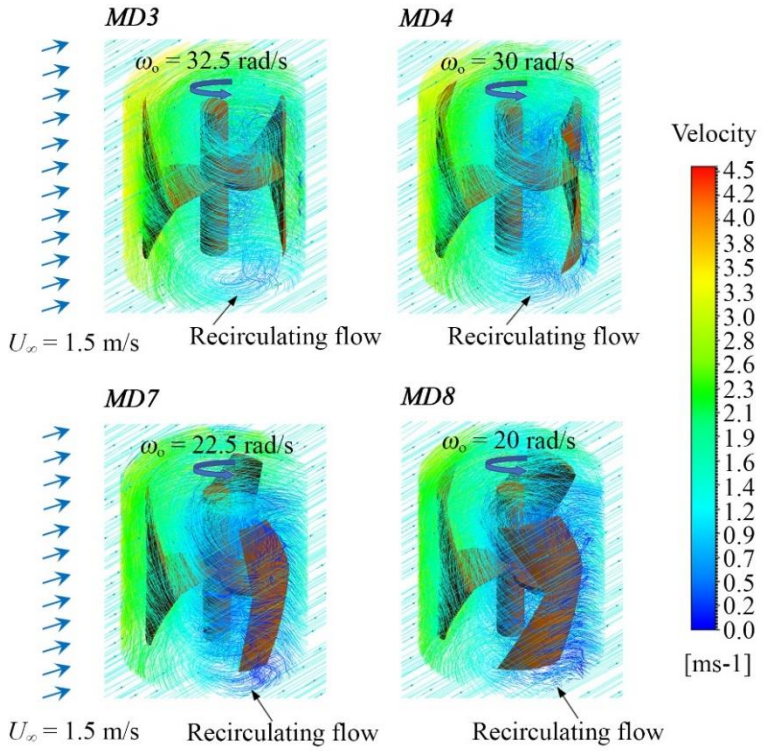

Figure 14. Isometric views inside the inner domain surrounded by velocity streamlines of *MD3*, *MD4*, *MD7*, and *MD8* at the maximum operational condition

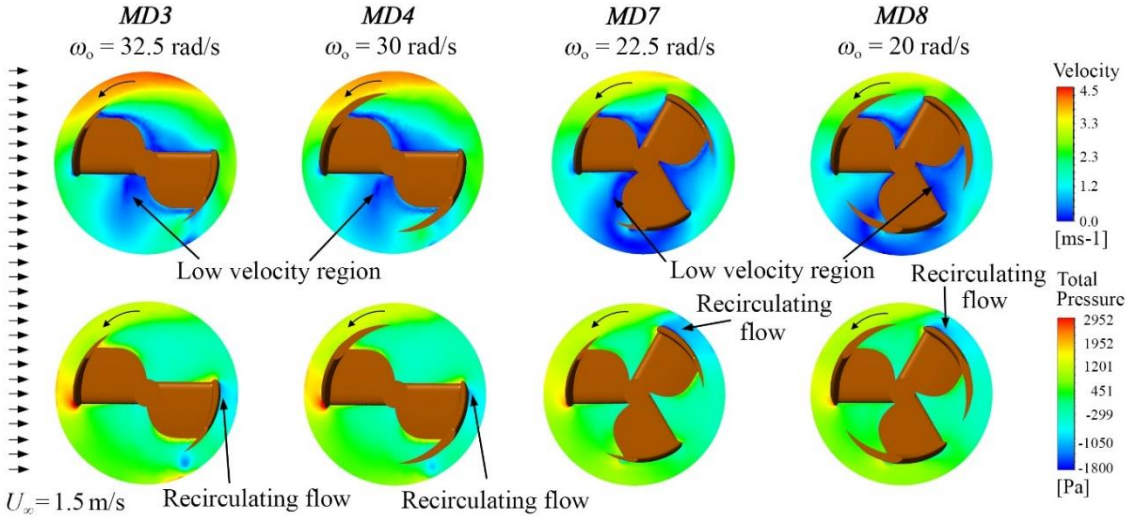

Figure 15. Sectional velocity and total pressure contours of *MD3*, *MD4*, *MD7*, and *MD8* at the maximum operational condition

As clearly seen in Figure 15, it was found that flow recirculation areas were observed to be bigger and wider for the 3-bladed models. The low velocity of water flows inside the 3-bladed models was seen clearly. When the models rotated, it acted as an obstruction where water could not flow through its blades. This was the reason why the maximum c_p of the 3-bladed models was lower than that of the 2-bladed designs.

7.0 CONCLUSIONS

To evaluate the design factors including bladed characteristics (in-plane, and twisted blade), bladed cross-sectional areas, as well as number of blades of the newly designed delta-shaped bladed Darrieus hydrokinetic turbine (DHKT), the simulation processes using the ANSYS Fluent CFD method were carried out systematically. The turbine performances represented by power and torque coefficient were computed and plotted. Simulation results from this study were compared with the previous numerical and experimental studies.

The processes were conducted to determine model designs of 2-bladed models, *MD1* - *MD4*. It was found that *MD1* and *MD2* models which were in-plane blades with reduced and constant cross-sectional areas, provided negative torque,

c_p and c_t because of their physical designs, while the twisted delta-shaped bladed models with reduced and constant cross-sectional area blades, *MD3* and *MD4* have positive ones. Therefore, the suitable designs for 2-bladed models were *MD3* and *MD4*, and they were selected to continue with further investigation on the effect of the number of blades.

The simulation results of 3-bladed models (*MD7*, and *MD8*) were plotted and compared with 2-bladed models (*MD3*, and *MD4*). The results showed that the 2-bladed models performed better during a higher range of λ. In contrast, the 3-bladed models showed better results during a lower range of λ. In addition, the cross-sectional areas of turbine blades affected the blade performance slightly. During a low range λ, the models with constant cross-sectional area blades, *MD4* and *MD8* showed higher c_p and c_t, while the reduced cross-sectional area design, *MD3* and *MD7* showed higher c_p and c_t during a high range of λ. Based on the simulation results, the twisted blade DHKT model with constant cross-sectional areas (*MD4*) was the most appropriate design for operating under the specified conditions.

8.0 ACKNOWLEDGEMENT

The authors would like to thank the sponsorship of the Southeast Asian Regional Center for Graduate Study and Research in Agriculture (SEARCA) and support from the CAD/CAM Laboratory, Faculty of Engineering, Universiti Putra Malaysia.

9.0 REFERENCES

[1] P. K. Yadav, A. Kumar, and S. Jaiswal, "A critical review of technologies for harnessing the power from flowing water using a hydrokinetic turbine to fulfill the energy need," *Energy Reports*, vol. 9, pp. 2102-2117, 2023,

[2] M. Sood and S. K. Singal, "Development of hydrokinetic energy technology: A review," *International Journal of Energy Research*, vol. 43, no. 11, pp. 5552-5571, 2019,

[3] W. I. Ibrahim, M. R. Mohamed, R. M. T. R. Ismail, P. K. Leung, W. W. Xing, and A. A. Shah, "Hydrokinetic energy harnessing technologies: A review," *Energy Reports*, vol. 7, pp. 2021-2042, 2021,

[4] M. El-Sawy, A. S. Shehata, A. A. Elbatran, and A. Tawfiq, "Numerical simulation of flow in hydrokinetic turbine channel to improve its efficiency by using first and second-law efficiency analysis," *Ocean Engineering*, vol. 244, p. 110400, 2022,

[5] A. Ali, J. Yuan, H. Javed, Q. Si, I. Fall, I. Ohiemi et al., "Small hydropower generation using pump as turbine; a smart solution for the development of Pakistan's energy," *Heliyon*, vol. 9, no. 4, p. e14993, 2023,

[6] A. Kumar and R. P. Saini, "Performance parameters of Savonius type hydrokinetic turbine – A Review," *Renewable and Sustainable Energy Reviews*, vol. 64, pp. 289-310, 2016,

[7] M. I. Yuce and A. Muratoglu, "Hydrokinetic energy conversion systems: A technology status review," *Renewable and Sustainable Energy Reviews*, vol. 43. pp. 72-82, 2015.

[8] K. Tantichukiad, A. Yahya, A. Mohd Mustafah, A. S. Mohd Rafie, and A. S. Mat Su, "Design evaluation reviews on the savonius, darrieus, and combined savonius-darrieus turbines," *Proceedings of the Institution of Mechanical Engineers, Part A: Journal of Power and Energy*, vol. 237, no. 6, pp. 1348-1366, 2023,

[9] A. Janon, "Torque coefficient analysis of a novel direct-drive parallel-stream counter-rotating darrieus turbine system," *Renewable Energy*, vol. 147, pp. 110-117, 2020,

[10] R. Gupta and K. K. Sharma, "Flow physics of a combined darrieus-savonius rotor using computational fluid dynamics (CFD)," *International Research Journal of Engineering Science, Technology and Innovation*, vol. 1, no. 1, pp. 1-13, 2012.

[11] M. T. Tigabu, M. S. U. Khalid, D. Wood, and B. T. Admasu, "Some effects of turbine inertia on the starting performance of vertical-axis hydrokinetic turbine," *Ocean Engineering*, vol. 252, p. 111143, 2022,

[12] Z. Kong, D. Zhou, and X. Sun, "Improvement of self-starting and power extraction performance of an H-type vertical-axis hydrokinetic turbine by partial deflection of its blades," *Ocean Engineering*, vol. 296, p. 116855, 2024,

[13] W. Tian, B. Song, and Z. Mao, "Conceptual design and numerical simulations of a vertical axis water turbine used for underwater mooring platforms," *International Journal of Naval Architecture and Ocean Engineering*, vol. 5, no. 4, pp. 625–634, 2013,

[14] I. S. Hwang, Y. H. Lee, and S. J. Kim, "Optimization of cycloidal water turbine and the performance improvement by individual blade control," *Applied Energy*, vol. 86, no. 9, pp. 1532–1540, 2009,

[15] S. Jain and U. K. Saha, "On the influence of blade thickness-to-chord ratio on dynamic stall phenomenon in H-type Darrieus wind rotors," *Energy Conversion and Management*, vol. 218, p. 113024, 2020,

[16] M. H. Mohamed, "Performance investigation of H-rotor Darrieus turbine with new airfoil shapes," *Energy*, vol. 47, no. 1, pp. 522–530, 2012,

[17] S. Yagmur and F. Kose, "Numerical evolution of unsteady wake characteristics of H-type Darrieus Hydrokinetic Turbine for a hydro farm arrangement," *Applied Ocean Research*, vol. 110, p. 102582, 2021,

[18] V. Patel, T. I. Eldho, and S. V. Prabhu, "Experimental investigations on Darrieus straight blade turbine for tidal current application and parametric optimization for hydro farm arrangement," *International Journal of Marine Energy*, vol. 17, pp. 110–135, 2017,

[19] A. Subramanian, S. A. Yogesh, H. Sivanandan, A. Giri, M. Vasudevan, V. Mugundhan et al., "Effect of airfoil and solidity on performance of small scale vertical axis wind turbine using three dimensional CFD model," *Energy*, vol. 133, pp. 179–190, 2017,

[20] M. H. Mohamed, A. M. Ali, and A. A. Hafiz, "CFD analysis for H-rotor Darrieus turbine as a low speed wind energy converter," *Engineering Science and Technology, an International Journal*, vol. 18, no. 1, pp. 1–13, 2015,

[21] M. Asadbeigi, F. Ghafoorian, M. Mehrpooya, S. Chegini, and A. Jarrahian, "A 3D Study of the Darrieus Wind Turbine with Auxiliary Blades and Economic Analysis Based on an Optimal Design from a Parametric Investigation," *Sustainability*, vol. 15, no. 5, p. 4684, 2023,

[22] N. Guillaud, G. Balarac, E. Goncalvès, and J. Zanette, "Large Eddy Simulations on Vertical Axis Hydrokinetic Turbines - Power coefficient analysis for various solidities," *Renewable Energy*, vol. 147, pp. 473-486, 2020,

[23] S. Armstrong, A. Fiedler, and S. Tullis, "Flow separation on a high Reynolds number, high solidity vertical axis wind turbine with straight and canted blades and canted blades with fences," *Renewable Energy*, vol. 41, pp. 13-22, 2012,

[24] Y. T. Lee and H. C. Lim, "Numerical study of the aerodynamic performance of a 500W Darrieus-type vertical-axis wind turbine," *Renewable Energy*, vol. 83, pp. 407-415, 2015,

[25] Q. Li, T. Maeda, Y. Kamada, K. Shimizu, T. Ogasawara, A. Nakai, et al., "Effect of rotor aspect ratio and solidity on a straight-bladed vertical axis wind turbine in three-dimensional analysis by the panel method," *Energy*, vol. 121, pp. 1-9, 2017,

[26] A. R. Sengupta, A. Biswas, and R. Gupta, "Studies of some high solidity symmetrical and unsymmetrical blade H-Darrieus rotors with respect to starting characteristics, dynamic performances and flow physics in low wind streams," *Renewable Energy*, vol. 93, pp. 536-547, 2016,

[27] E. Singh, S. Roy, K. S. Yam, and M. C. Law, "Numerical analysis of H-Darrieus vertical axis wind turbines with varying aspect ratios for exhaust energy extractions," *Energy*, vol. 277, p. 127739, 2023,

[28] M. Ghasemian, Z. N. Ashrafi, and A. Sedaghat, "A review on computational fluid dynamic simulation techniques for Darrieus vertical axis wind turbines," *Energy Conversion and Management*, vol. 149, pp. 87-100, 2017,

[29] R. Kumar and S. Sarkar, "Effect of design parameters on the performance of helical Darrieus hydrokinetic turbines," *Renewable and Sustainable Energy Reviews*, vol. 162, p. 112431, 2022,

[30] Y. Chen, J. Su, Z. Han, *et al.*, "A shape optimization of ϕ-shape Darrieus wind turbine under a given range of inlet wind speed," *Renewable Energy*, vol. 159, pp. 286-299, 2020,

[31] M. H. Mohamed, "Criticism study of J-Shaped darrieus wind turbine: Performance evaluation and noise generation assessment," *Energy*, vol. 177, pp. 367-385, 2019,

[32] R. Farzadi and M. Bazargan, "3D numerical simulation of the Darrieus vertical axis wind turbine with J-type and straight blades under various operating conditions including self-starting mode," *Energy*, vol. 278, p. 128040, 2023,

[33] A. García Auyanet, R. E. Santoso, H. Mohan, S. S. Rathore, D. Chakraborty, and P. G. Verdin, "CFD-Based J-Shaped Blade Design Improvement for Vertical Axis Wind Turbines," *Sustainability (Switzerland)*, vol. 14, no. 22, 2022,

[34] M. T. Asr, E. Z. Nezhad, F. Mustapha, and S. Wiriadidjaja, "Study on start-up characteristics of H-Darrieus vertical axis wind turbines comprising NACA 4-digit series blade airfoils," *Energy*, vol. 112, pp. 528-537, 2016,

[35] A. Arab, M. Javadi, M. Anbarsooz, and M. Moghiman, "A numerical study on the aerodynamic performance and the self-starting characteristics of a Darrieus wind turbine considering its moment of inertia," *Renewable Energy*, vol. 107, pp. 298-311, 2017,

[36] B. Hand and A. Cashman, "A review on the historical development of the lift-type vertical axis wind turbine: From onshore to offshore floating application," *Sustainable Energy Technologies and Assessments*, vol. 38, p. 100646, 2020,

[37] S. M. H. Karimian and A. Abdolahifar, "Performance investigation of a new Darrieus Vertical Axis Wind Turbine," *Energy*, vol. 191, p. 116551, 2020,

[38] O. S. Mohamed, A. A. Ibrahim, A. K. Etman, A. A. Abdelfatah, and A. M. R. Elbaz, "Numerical investigation of Darrieus wind turbine with slotted airfoil blades," *Energy Conversion and Management: X*, vol. 5, 2020,

[39] A. Abdolahifar and S. M. H. Karimian, "A comprehensive three-dimensional study on Darrieus vertical axis wind turbine with slotted blade to reduce flow separation," *Energy*, vol. 248, p. 123632, 2022,

[40] C. Attie, A. ElCheikh, J. Nader, and M. Elkhoury, "Performance enhancement of a vertical axis wind turbine using a slotted deflective flap at the trailing edge," *Energy Conversion and Management*, vol. 273, p. 116388, 2022,

[41] W. Hao, M. Bashir, C. Li, and C. Sun, "Flow control for high-solidity vertical axis wind turbine based on adaptive flap," *Energy Conversion and Management*, vol. 249, p. 114845, 2021,

[42] M. Yousefi Roshan, J. Khaleghinia, M. Eshagh Nimvari, and H. Salarian, "Performance improvement of Darrieus wind turbine using different cavity layouts," *Energy Conversion and Management*, vol. 246, p.114693, 2021,

[43] A. A. Ibrahim, A. M. R. Elbaz, P. F. Melani, O. S. Mohamed, and A. Bianchini, "Power augmentation of Darrieus wind turbine blades using trapped vortex cavity," *Journal of Wind Engineering and Industrial Aerodynamics*, vol. 223, p. 104949, 2022,

[44] H. Sedighi, P. Akbarzadeh, and A. Salavatipour, "Aerodynamic performance enhancement of horizontal axis wind turbines by dimples on blades: Numerical investigation," *Energy*, vol. 195, p. 117056, 2020,

[45] A. Eltayesh, F. Castellani, F. Natili, M. Burlando, and A. Khedr, "Aerodynamic upgrades of a Darrieus vertical axis small wind turbine," *Energy for Sustainable Development*, vol. 73, pp. 126-143, 2023,

[46] Y. Yan, E. Avital, J. Williams, and J. Cui, "Aerodynamic performance improvements of a vertical axis wind turbine by leading-edge protuberance," *Journal of Wind Engineering and Industrial Aerodynamics*, vol. 211, p. 104535, 2021,

[47] A. Bianchini, F. Balduzzi, D. Di Rosa, and G. Ferrara, "On the use of Gurney Flaps for the aerodynamic performance augmentation of Darrieus wind turbines," *Energy Conversion and Management*, vol. 184, pp. 402-415, 2019,

[48] L. Ni, W. Miao, C. Li, and Q. Liu, "Impacts of Gurney flap and solidity on the aerodynamic performance of vertical axis wind turbines in array configurations," *Energy*, vol. 215, p. 118915, 2021,

[49] M. A. Singh, A. Biswas, and R. D. Misra, "Investigation of self-starting and high rotor solidity on the performance of a three S1210 blade H-type Darrieus rotor," *Renewable Energy*, vol. 76, pp. 381-387, 2015,

[50] X. Liang, S. Fu, B. Ou, C. Wu, C. Y. H. Chao, and K. Pi, "A computational study of the effects of the radius ratio and attachment angle on the performance of a Darrieus-Savonius combined wind turbine," *Renewable Energy*, vol. 113, pp. 329-334, 2017,

[51] F. Scheurich and R. E. Brown, "Modelling the aerodynamics of vertical-axis wind turbines in unsteady wind conditions," *Wind Energy*, vol. 16, no. 1, pp. 91–107, 2013,

[52] F. Scheurich, T. M. Fletcher, and R. E. Brown, "The Influence of Blade Curvature and Helical Blade Twist on the Performance of a Vertical-Axis Wind Turbine," *29th ASME Wind Energy Symposium*, Orlando, Florida: the American Institute of Aeronautics and Astronautics, Inc., 2010, pp. 1–16. Accessed: Jan. 07, 2010. [Online]. Available: http://strathprints.strath.ac.uk/27341/

[53] S. Laín, P. Cortés, and O. D. López, "Numerical simulation of the flow around a straight blade Darrieus water turbine," *Energies*, vol. 13, no. 5, p. 1137, 2020,

[54] S. Yagmur, F. Kose, and S. Dogan, "A study on performance and flow characteristics of single and double H-type Darrieus turbine for a hydro farm application," *Energy Conversion and Management*, vol. 245, p. 114599, 2021,

[55] M. N. Doan, Y. Kai, and S. Obi, "Twin marine hydrokinetic cross-flow turbines in counter rotating configurations: A laboratory-scaled apparatus for power measurement," *Journal of Marine Science and Engineering*, vol. 8, no. 11, pp. 1-16, 2020,

[56] A. Dessoky, T. Lutz, and E. Krämer, "Aerodynamic and aeroacoustic performance investigations on modified H-rotor Darrieus wind turbine," *Wind Engineering*, vol. 46, no. 1, pp. 69-88, 2022,

[57] R. Ansaf, H. S. Abdelhameed, I. Hashem, and Z. Harun, "Efficiency-based design optimization of the H-type Darrieus wind turbine with fixed guiding-walls," *Energy Reports*, vol. 9, pp. 3576–3592, 2023,

[58] I. F. Zidane, H. M. Ali, G. Swadener, Y. A. Eldrainy, and A. I. Shehata, "Effect of upstream deflector utilization on H-Darrieus wind turbine performance: An optimization study," *Alexandria Engineering Journal*, vol. 63, pp. 175-189, 2023,

[59] F. Arpino, M. Scungio, and G. Cortellessa, "Numerical performance assessment of an innovative Darrieus-style vertical axis wind turbine with auxiliary straight blades," *Energy Conversion and Management*, vol. 171, pp. 769-777, 2018,

[60] F. Arpino, G. Cortellessa, M. Scungio, G. Fresilli, A. Facci, and A. Frattolillo, "PIV measurements over a double bladed Darrieus-type vertical axis wind turbine: A validation benchmark," *Flow Measurement and Instrumentation*, vol. 82, p. 102064, 2021,

[61] M. Ahmad, A. Shahzad, F. Akram, F. Ahmad, and S. I. A. Shah, "Design optimization of Double-Darrieus hybrid vertical axis wind turbine," *Ocean Engineering*, vol. 254, p. 111171, 2022,

[62] Z. Shen, S. Gong, G. Xie, H. Lu, and W. Guo, "Investigation of the effect of critical structural parameters on the aerodynamic performance of the double darrieus vertical axis wind turbine," *Energy*, vol. 290, p. 130156, 2024,

[63] A. Hosseini and N. Goudarzi, "Design and CFD study of a hybrid vertical-axis wind turbine by employing a combined Bach-type and H-Darrieus rotor systems," *Energy Conversion and Management*, vol. 189, pp. 49-59, 2019,

[64] K. H. Wong, W. T. Chong, S. C. Poh, Y. C. Shiah, N. L. Sukiman, and C. T. Wang, "3D CFD simulation and parametric study of a flat plate deflector for vertical axis wind turbine," *Renewable Energy*, vol. 129, pp. 32-55, 2018,